This is an open access article published under a Creative Commons Attribution (CC-BY) License, which permits unrestricted use, distribution and reproduction in any medium, provided the author and source are cited.

LANGMUIR Article
Cite This: Langmuir 2019, 35, 4577−4588
pubs.acs.org/Langmuir

Atmospheric Pressure Plasma-Synthesized Gold Nanoparticle/Carbon Nanotube Hybrids for Photothermal Conversion

Daye Sun,[†] James McLaughlan,[‡,§] Li Zhang,[∥] Brian G. Falzon,[†] Davide Mariotti,[⊥] Paul Maguire,[⊥] and Dan Sun*[,†]

[†]Advanced Composites Research Group (ACRG), School of Mechanical and Aerospace Engineering, Queen's University, Belfast BT9 5AH, U.K.
[‡]School of Electronic and Electrical Engineering and [§]Leeds Institute of Medical Research, University of Leeds, Leeds LS2 9JT, U.K.
[∥]Research Center for Nano−Biomaterials, Analytical & Testing Center, Sichuan University, Chengdu 610065, China
[⊥]Nanotechnology and Integrated Bioengineering Centre (NIBEC), Ulster University, Newtownabbey BT37 0QB, U.K.

Supporting Information

ABSTRACT: In this work, a room-temperature atmospheric pressure direct-current plasma has been deployed for the one-step synthesis of gold nanoparticle/carboxyl group-functionalized carbon nanotube (AuNP/CNT-COOH) nanohybrids in aqueous solution for the first time. Uniformly distributed AuNPs are formed on the surface of CNT-COOH, without the use of reducing agents or surfactants. The size of the AuNP can be tuned by changing the gold salt precursor concentration. UV−vis, ζ-potential, and X-ray photoelectron spectroscopy suggest that carboxyl surface functional groups on CNTs served as nucleation and growth sites for AuNPs and the multiple potential reaction pathways induced by the plasma chemistry have been elucidated in detail. The nanohybrids exhibit significantly enhanced Raman scattering and photothermal conversion efficiency that are essential for potential multimodal cancer treatment applications.

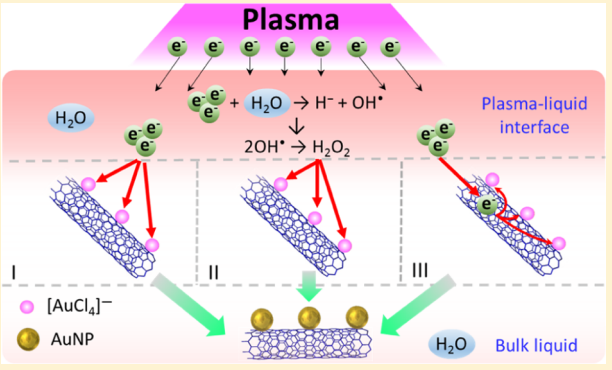

INTRODUCTION

Gold nanoparticles (AuNPs) are currently approved by the Food and Drug Administration (FDA)[1] for noninvasive biomedical applications and have been widely explored in cancer treatment for drug delivery, bio-imaging, diagnose, and photothermal therapy (PTT) because of their unique physical/chemical properties and high biocompatibility.[2−5] Nano-carbon-based materials, such as graphene, graphene oxide, and carbon nanotubes (CNTs), on the other hand, have also been explored for a wide range of healthcare applications including cancer diagnostics, treatment, and sensing.[6−9] CNTs, in particular, have gained increasing attention in cancer therapies for the delivery of anticancer drugs, hyperthermia, and bio-imaging in virtue of their unique structural, thermal, and chemical properties.[10−12] For instance, CNTs can effectively accumulate in tumor cells/tissues because of their enhanced permeability and retention effects induced by the defectiveness, leakage, and abnormalities in tumor cells/tissues.[13−15] Although the toxicity issue of CNTs remains controversial, it is believed to be closely related to the dosage used as well as the structure/properties of the CNTs (such as length, diameter, alignment, and degree of entanglement surface functionalities.[16,17]) and therefore cannot be generalized.[18−21] For these reasons, further efforts are still required to control the dosage-related toxicity of CNTs and to improve the tumor-targeting efficiency of AuNPs in cancer applications.[14,22] The creation of AuNP/CNT hybrid nanosystems with enhanced opto-thermic properties may offer the opportunity to address these specific challenges, for instance by reducing the dosage. In this sense, fundamental opto-thermic properties of AuNP/CNT hybrids are very important and can be used to optimize the nano-systems and assess initial viability. This approach avoids carrying out full and extensive toxicity studies on a very large range of morphologies, chemical compositions, configurations and so forth. Such hybrid may also potentially serve as a new nanomedicine platform providing multi-theranostic functions including cellular imaging/detection, PTT, and cancer drug delivery.[23−27]

Several strategies have been attempted for the synthesis of AuNP/CNT nanohybrids. Wet chemistry-based synthesis is one of the most common approaches, where harsh/hazardous reducing chemicals (such as sodium borohydride) are normally required.[28] Although greener reducing agents (such as gallic acid) have been proposed, wet chemistry-based synthesis still

Received: November 26, 2018
Revised: January 17, 2019
Published: March 6, 2019

Downloaded via UNIV OF STRATHCLYDE on May 21, 2024 at 10:01:11 (UTC).
See https://pubs.acs.org/sharingguidelines for options on how to legitimately share published articles.

remains laborious and mostly require elevated temperature, long processing time, and cumbersome cleansing processes.[29] Raghuveer et al. proposed microwave-assisted chemical reduction routines, which could markedly reduce the reaction time; however, harsh reducing agents and potentially hazardous radiation source are inevitable.[30] Alternative methods, such as solid-state thermal evaporation or sputtering require more sophisticated facilities and AuNPs that formed randomly on the CNT surfaces are often aggregated.[31] The hybridizing of CNTs with AuNPs can also be achieved via electrochemical or electroless deposition, however, in both cases CNTs need to be immobilized on a substrate.[32,33]

The application of AuNP/CNT hybrids specifically for cancer treatments has favored other more recent synthesis techniques. Layer-by-layer (LbL) assembly has been the main technique deployed to date.[23−27] The LbL technique involves multiple steps which normally starts with functionalization of CNTs surfaces with polymers, biomacromolecule, or thiols to form an intermediated layer. The surface-modified CNTs are then either hybridized with presynthesized AuNPs through the electrostatic interaction[23,25,26] or AuNPs formed in situ via conventional chemical reduction method.[24,27] Many of these hybrid structures feature heavily aggregated AuNP (with varying size and morphology) coated on the CNT surface. The effects of AuNP size and the process−structure−property relationship with respect to the synthesis of such hybrid structures have not been well established in the context of cancer treatment.

Nonequilibrium atmospheric pressure plasma (APP) and in particular APP−liquid interactions, have demonstrated exceptional versatility in the synthesis and surface engineering of nanomaterials.[34−39] When interacting with water, a high density of gas phase plasma electrons become solvated in the liquid, creating a rapid cascade of transient nonlinear chemical reactions and highly reactive radicals (e.g., $H^{\bullet}$ and $OH^{\bullet}$).[40,41] Solvated electrons and/or reactive species are responsible for the successful synthesis of various nanomaterials, such as AuNPs, AgNPs, Fe_3O_4 NPs, Cu_2O NPs, and alloyed NPs such as Au_xAg_{1-x} in aqueous solutions.[42−46]

In this work, we report the proof-of-concept of using of a facile and rapid direct current room temperature APP technique for the one-step synthesis of AuNP/CNT nanohybrids in aqueous solution. Stable and uniformly dispersed hybrid samples can be achieved unhindered by the use of solvents and surfactants. Great insight has been developed for the interfacial interaction between AuNPs and CNTs with different surface functionalities, enabling the identification of the underlining mechanisms of different photothermal conversion capabilities seen in AuNP/CNT hybrid systems. The study also helps to establish the "process−structure−property relationship", which may provide important guidance for optimizing the future fabrication process of a wide range of nanocomposite/hybrid materials for healthcare applications and beyond.

EXPERIMENTAL SECTION

Materials. Three different types of surface-functionalized multiwall CNTs were purchased from Cheap Tubes Inc., including carboxyl (−COOH)-functionalized CNT with higher (1.2%) −COOH density (namely CNT-COOH-H, purity > 95 wt %, length 10−30 μm, diameter 20−30 nm, according to manufacturer's data sheet), carboxyl (−COOH)-functionalized CNT with lower (0.73%) −COOH density (namely CNT-COOH-L, purity > 95 wt %, length 0.5−2.0 μm, diameter 30−50 nm), and hydroxyl (−OH)-functionalized CNT with 1.0% OH density (namely, CNT-OH, purity > 95 wt %, length 0.5−2.0 μm, diameter 30−50 nm). $HAuCl_4$ aqueous solutions (2.5 μM, 0.1 mM, and 0.2 mM) were prepared by mixing chloroauric acid trihydrate ($HAuCl_4{\cdot}3H_2O$, > 99.9%, Sigma-Aldrich) with appropriate amount of deionized water [Millipore Milli-Q machine (18.2 $M\Omega{\cdot}cm^{-1}$)].

APP Setup. The APP setup deployed in this work, as shown in Scheme 1, consists of a graphite rod as the anode and a stainless-steel capillary (250 μm inner diameter) as the cathode. The graphite rod was immersed in the aqueous solution, while the stainless steel capillary was placed approx. 1 mm above the liquid surface. The approximate distance between the anode and cathode was 2 cm. Helium (He) gas (25 sccm flow rate) was supplied through the capillary and the plasma can be triggered and maintained at ∼2 kV voltage and 5 mA current. All samples mentioned in this work were treated for 10 min under a static condition.

Scheme 1. Diagram of the APP Setup

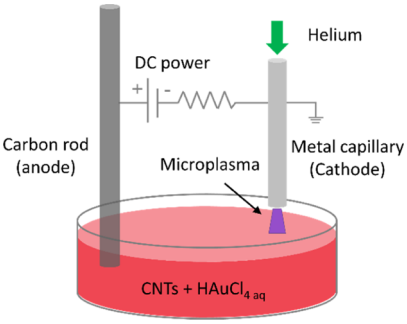

Synthesis of AuNP/CNT Hybrids. CNTs/water mixture (0.1 mg/mL) was sonicated (140 W) for 6 h and centrifuged at 5000 rpm for 4 h, and the supernatant with dispersed CNTs was collected. The supernatants were diluted by adding appropriate amount of deionized water to obtain dispersed CNT solutions with a concentration of 50 ± 3 μg/mL. An appropriate amount of concentrated (5 mM) $HAuCl_4$ solution was added to different CNT dispersion samples, to obtain aqueous mixtures of CNT with different $HAuCl_4$ concentrations (2.5 μM, 0.1, and 0.2 mM were used in this work). The resultant mixtures were settled for 0.5 h prior to APP processing.

The samples were named after the type of CNT functional groups and the $HAuCl_4$ precursor concentration used (see Table 1) and all samples were stored in glass vials (see Figure S1 in Supporting Information); for comparison and to provide further details for the discussion and analysis, a range of other samples were considered and these are summarized in Table 2.

Table 1. Nomenclatures of Samples and Their Preparation Methods

samples	CNTs used	precursor used	APP
CNT-COOH-H	as purchased, 1.2% −COOH density	none	no
2.5 μM AuNP/CNT-COOH-H	CNT-COOH-H	2.5 μM $HAuCl_4$	yes
0.1 mM AuNP/CNT-COOH-H	CNT-COOH-H	0.1 mM $HAuCl_4$	yes
0.2 mM AuNP/CNT-COOH-H	CNT-COOH-H	0.2 mM $HAuCl_4$	yes

Characterization. Ultraviolet−visible (UV−vis) absorption spectra of the solutions were recorded using an Agilent spectrometer (Cary 60 UV−Vis, Agilent Technologies). The morphologies and sizes of the nanostructures were investigated by transmission electron microscopy (TEM; Philips Tecnai F20D), along with ImageJ software for the particle size analysis (more than 100 particles were analyzed).

DOI: 10.1021/acs.langmuir.8b03945
Langmuir 2019, 35, 4577−4588

Table 2. Nomenclatures of Other Samples for Comparison and Their Preparation Methods

sample	CNTs used	precursor used	APP
CNT-COOH-L	as purchased, 0.73% −COOH density	none	no
CNT-OH	as purchased, 1.0% −OH density	none	no
0.1 mM AuNP/CNT-COOH-L	CNT-COOH-L	0.1 mM $HAuCl_4$	yes
0.1 mM AuNP/CNT-OH	CNT-OH	0.1 mM $HAuCl_4$	yes
2.5 μM AuNP	none	2.5 μM $HAuCl_4$	yes
0.1 mM AuNP	none	0.1 mM $HAuCl_4$	yes
0.2 mM AuNP	none	0.2 mM $HAuCl_4$	yes

Samples for TEM characterization were all prepared by depositing a 25 μL droplet of sample solution onto a TEM sample grid. ζ-potential measurements were carried out using a zeta potential analyzer (Omni, Brookhaven). X-ray photoelectron spectroscopy (XPS) results were obtained from a Kratos Axis Ultra XPS system (monochromatic Al Kα X-rays, 1486 eV), which was run at a current of 10 mA and a voltage of 15 kV, respectively. The conducting environment base pressure was 1×10^{-9} mbar. The samples were prepared by drop casting aqueous solutions on neat and intrinsic silicon wafer and thoroughly dried under room temperature. High-resolution (0.05 eV) XPS spectra including C 1s and Au 4f peaks were performed at a pass energy of 40 eV. The C 1s peak located at 284.5 eV was used for the calibration of the obtained spectra. An open source software (CasaXPS) was deployed for the data analysis. Samples for Raman analysis were prepared by drop casting 100 μL of the liquid sample on neat and intrinsic silicon wafer with a prefabricated 6 mm × 6 mm square well. After completely drying under room temperature, Raman scattering spectra of all samples were measured under ambient conditions by Raman spectroscopy (LabRAM 300, Horiba, UK with a 632 nm N_2−H_2 laser excitation source). The output of the laser box was 3.7 kV and 7 mA, and 1% of the output was chosen for characterization. Each scan was divided into three segments with a total illumination time of 45 s.

Photothermal Conversion Tests. The photothermal effect of the hybrids was tested under the irradiation of an 852 nm continuous wavelength (CW) diode laser source with a power of 1.5 W (B4-852-1500-15C, Sheaumann Laser Inc). Each solution (100 μL) was placed in a 96-well plated container, which was irradiated by the laser, and the temperature of the solution was monitored by an IR temperature sensor (CSL-CF2 High-performance pyrometer, Micro-Epsilon).

RESULTS AND DISCUSSION

The optical properties of all samples were analyzed by UV−vis spectroscopy, see Figure 1. The APP treatment had no influence on the absorption spectra of the CNT-COOH-H when they were processed without adding $HAuCl_4$. However, for samples containing $HAuCl_4$, APP treatment had led to a well-dispersed colloid solution with changed color (Figure S1, Supporting Information), indicating the formation of AuNP with different particle sizes.[36,42] The emergence of peaks at 531 nm for 0.1 mM AuNP/CNT-COOH-H and 554 nm for 0.2 mM AuNP/CNT-COOH-H shown in Figure 1 can be attributed to the typical localized surface plasmon resonance (LSPR) effects of AuNPs.[47] The red shift of the LSPR peak can be related to the increase of the NP size as a result of greater $HAuCl_4$ concentration.[48] However, the LSPR peak for the 2.5 μM AuNP/CNT-COOH-H hybrid is not visible. With very low gold precursor concentration (2.5 μM), the plasmonic

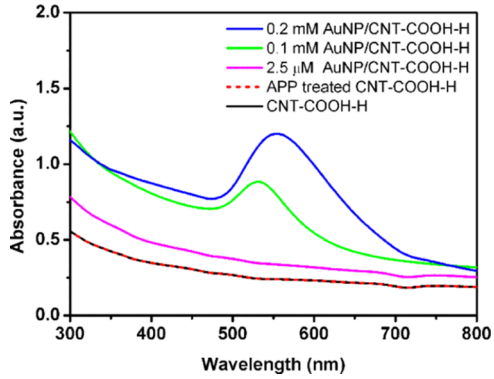

Figure 1. UV−vis spectra of the untreated CNT-COOH-H, APP treated CNT-COOH-H, and in situ synthesized AuNP/CNT-COOH-H hybrids.

absorption may be very low because of the very low concentration of the synthesized AuNPs.

The morphologies of the AuNP/CNT-COOH-H hybrids have been investigated by TEM, see Figure 2. CNT-COOH-H after plasma treatment do not show any morphological changes (e.g., length; see also Figure S2 in Supporting Information for TEM of untreated CNT-COOH-H). However, AuNPs are found to attach on CNT surfaces without obvious agglomerations, demonstrating that the plasma-induced liquid chemistry is effective in producing AuNP/CNT-COOH-H hybrids. As it is shown in Figure 2A−C, the AuNPs within all the nanohybrids are mostly spherical (the shape projections of AuNP within AuNP/CNT-COOH hybrids can be found in Figure S3, Supporting Information), though NPs in the 0.2 mM AuNP/CNT-COOH-H hybrids start to show signs of heterogeneous growth (e.g., triangles, rods, and so forth, also see Figure S3 in Supporting Information). In contrast, pure AuNPs synthesized under the same plasma conditions (i.e., without the presence of CNT-COOH-H and using the respective $HAuCl_4$ concentrations) tend to exhibit more irregular shapes (e.g., triangles, hexagons, and rods) (see the shape projections of AuNPs in Figure S4A−C, Supporting Information). Detailed examination of each sample (Figure 2A−C insets) suggests some form of interactions between AuNPs and CNT-COOH-H interface as, for all samples, there is no evidence of any AuNP remaining unattached. Particle sizes and distributions are analyzed by "ImageJ", and more than 100 NPs were studied for each sample. The size of spherical NPs is determined by diameter, while that of other shapes is determined by the longest length; the average size and distribution is fitted with a Gaussian function. As can be seen from Figure 2D, the average NP size (corresponding size distribution can be seen in Figure S3) increases with increasing $HAuCl_4$ concentration, which is consistent with the UV−vis results discussed earlier (Figure 1).

In order to gain more insight into the chemical composition and bonding arrangements, a comparison of the element chemical states between the untreated CNT-COOH-H and 0.1 mM AuNP/CNT-COOH-H hybrid was investigated by XPS, and the mediate mixture 0.1 mM $HAuCl_4$/CNT-COOH-H was considered for comparison. First, we looked at the difference between the survey spectra of CNT-COOH-H and 0.1 mM AuNP/CNT-COOH-H. As shown in Figure 3A, spectrum of the 0.1 mM AuNP/CNT-COOH-H hybrid showed distinct Au peaks and a significant decrease in the oxygen peak intensity, indicating the presence of Au element as

DOI: 10.1021/acs.langmuir.8b03945
Langmuir 2019, 35, 4577−4588

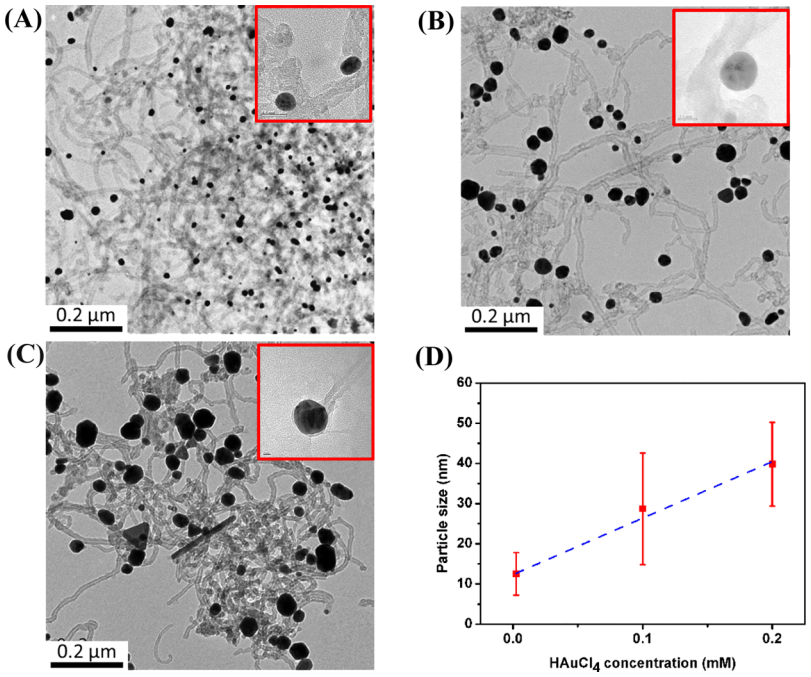

Figure 2. TEM images of AuNP/CNT-COOH-H synthesized from different HAuCl4 precursor concentrations (A) 2.5 μM, (B) 0.1, and (C) 0.2 mM AuNP/CNT-COOH-H hybrids, respectively; insets: corresponding higher magnification images; and (D) variations of average AuNPs particle sizes within the three hybrids.

compared to the pure CNT-COOH-H sample. High-resolution scan on C 1s and Au 4f spectra were then carried out to compare the changes in the states of elements for CNT-COOH-H, 0.1 mM $HAuCl_4$/CNT-COOH-H, and 0.1 mM AuNP/CNT-COOH-H after APP treatment. Before mixing with $HAuCl_4$ aqueous, there is no Au 4f peak detected for pure CNT-COOH-H as shown in the survey spectrum; the C 1s peak of pure CNT-COOH-H (Figure 3B) can be detected and deconvoluted into six components because of the different carbon elemental environments: the sp^2-hybridized carbon (C═C), the sp^3-hybridized carbon (C−C), the oxygen-containing functionalities including C−O, C═O, and O−C═O, and the satellite peak due to $\pi-\pi$ interactions.[49] When CNT-COOH-H was mixed with $HAuCl_4$ prior to the APP, an Au 4f peak emerged as shown in Figure 3C; the spectrum can be clearly fitted into two doublets centered at the binding energy (BE) of 84.7/88.3 and 86.9/90.6 eV that correspond to the BE of the ionic Au state, that is, Au^+ and Au^{3+} in the unreduced salt, respectively.[50−52] After being treated by APP, the Au 4f core spectrum of 0.1 mM AuNP/CNT-COOH-H presents two Au $4f_{7/2}$ and Au $4f_{5/2}$ core peaks centered at the BE of 84.0 and 87.7 eV, respectively; these two element states of Au 4f are in accordance with the profiles of reduced metallic Au^0.[53] The changes seen in the Au 4f states clearly indicate the formation of the AuNPs on CNT-COOH-H surfaces due to the reduction of ionic Au after the APP treatment. In addition, there are also some changes observed in the C 1s core peak of CNT-COOH-H following the mixing with $HAuCl_4$ as well as after the APP treatment. Specifically, the C 1s of the 0.1 mM $HAuCl_4$/CNT-COOH-H sample (Figure 3E) and the 0.1 mM AuNP/CNT-COOH-H sample (Figure 3F) can be both deconvoluted into six peaks, similar to that of the pure CNT-COOH-H sample; the detailed BE and percentage of each fitted peak for all samples are listed in Table 3. Compared to pure CNT-COOH-H, the fractions of oxygen-containing −C−O, −C═O and −O−C═O peaks all decreased significantly for both the 0.1 mM $HAuCl_4$/CNT-COOH-H mixture and the 0.1 mM AuNP/CNT-COOH-H hybrid C 1s peak. The result is consistent with the report by Suarez-Martinez et al., where AuNPs formed on the CNT with −COOH terminations had led to a decreased fraction of oxygen-containing carbon species in the C 1s core XPS peak.[54]

The formation mechanisms leading to reduction and growth of AuNPs can now be discussed. First, we should note that when the COOH-functionalized CNTs are dispersed in water, CNTs become negatively charged because of deprotonation and the surface terminations effectively become $-COO^-$.[55] At this point, the CNT aqueous dispersion has a pH of ∼6.3 and the ζ-potential is about −40 mV (Table 4), confirming the surface negative charge and stability of the colloid. Upon addition of the gold salt, the pH is immediately reduced to ∼2.3 and also the ζ-potential decreases in absolute values (Table 4). $HAuCl_4$ in water is present in its ionic state (i.e., $[AuCl_4]^- + H^+$), which justifies the acidity of the solution; here, the solution was not buffered at any point of the process and therefore we did not use the pH to control or vary reaction paths. It has been shown that $[AuCl_4]^-$ undergoes a partial reduction via ion exchange reaction on the CNT surface through chemical binding with the deprotonated $-COO^-$ terminations,[56,57] in particular

$$-COO^- + [AuCl_4]^- \rightarrow [-COOAuCl_3]^- + Cl^- \quad (1)$$

The reduction in the ζ-potential (in absolute values), as observed experimentally (Table 4), is the result of $-COO^-$ sites on the surface of CNTs that are now surrounded by Au^{3+}. UV−vis has been also used to support reaction 1, see Figure 4. For pure $HAuCl_4$ aqueous solution, two absorption bands are present at approximately 220 and 288 nm, corresponding to the $p_\pi 5d_{x^2-y^2}$ and $p_\sigma 5d_{x^2-y^2}$ ligand−metal transition modes in the $[AuCl_4]^-$ complex structures, respectively.[58] The absorp-

DOI: 10.1021/acs.langmuir.8b03945
Langmuir 2019, 35, 4577−4588

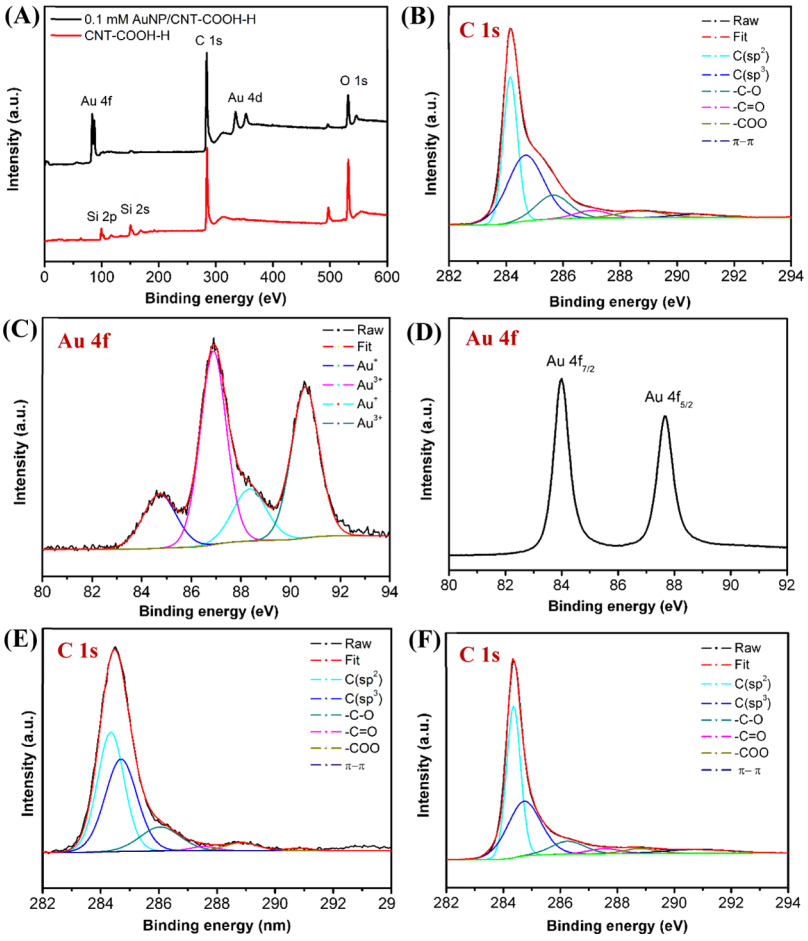

Figure 3. (A) Survey XPS spectra of untreated CNT-COOH-H and 0.1 mM AuNP/CNT-COOH-H hybrid; (B) C 1s core XPS spectrum of CNT-COOH-H; Au 4f core XPS spectrum of (C) 0.1 mM $HAuCl_4$/CNT-COOH-H mixture and (D) 0.1 mM AuNP/CNT-COOH-H hybrid; and C 1s core XPS spectrum of (E) 0.1 mM $HAuCl_4$/CNT-COOH-H mixture and (F) 0.1 mM AuNP/CNT-COOH-H hybrid.

Table 3. C 1s Peak Analysis Results for CNT-COOH-H, 0.1 mM $HAuCl_4$/CNT-COOH-H Mixture, and 0.1 mM AuNP/CNT-COOH-H Hybrid

samples		carbon species					
		C (sp^2)	C (sp^3)	C–O	C=O	O–C=O	π–π
CNT-COOH-H	BE (eV)	284.2	284.7	285.6	287.0	288.7	290.6
	fraction (%)	34.7	39.8	13.4	4.3	5.3	2.5
0.1 mM $HAuCl_4$/CNT-COOH-H	BE (eV)	284.3	284.7	286.0	287.5	288.8	290.8
	fraction (%)	42.3	39.1	12.7	1.5	3.5	0.9
0.1 mM AuNP/CNT-COOH-H	BE (eV)	284.4	284.7	286.3	287.6	288.8	290.8
	fraction (%)	42.6	36.6	8.7	3.5	3.4	5.2

Table 4. ζ-Potentials of the CNT-COOH-H Solutions before and after the Addition of $HAuCl_4$

samples	ζ-potential (mV, 25 °C)[a]
CNT-COOH-H	−40.46 ± 0.74
2.5 μM $HAuCl_4$/CNT-COOH-H	−31.60 ± 1.76
0.1 mM $HAuCl_4$/CNT-COOH-H	−26.39 ± 1.03
0.2 mM $HAuCl_4$/CNT-COOH-H	−23.37 ± 0.68

[a]Averaged values from five measurements.

tion peaks of free $[AuCl_4]^-$ (220 and 280 nm) both decreased and blue shifted when UV–vis was taken from the 0.1 mM $HAuCl_4$/CNT-COOH-H solution prior to APP processing. This transition can be attributed to the interaction between the $[AuCl_4]^-$ complex and the deprotonated carboxylic groups as per reaction 1.

Our results therefore corroborate surface reaction 1 whereby pH, ζ-potential, UV–vis, and also the reduction of the oxygen-containing carbon species in the C 1s core XPS peak (Table 3) are all in agreement with the literature.[54,57] It follows that the aqueous samples subjected to the plasma treatment are therefore formed by CNTs with a hybrid surface functionalization (i.e., $[-COOAuCl_3]^-$) and with the remaining of the gold salt still in solution. The subsequent formation of the AuNP has taken place through APP-induced chemistry, where we believe that $[-COOAuCl_3]^-$ on the surface of the CNTs served as preferential sites for further reduction and growth. We should note that the mechanisms leading to particle

DOI: 10.1021/acs.langmuir.8b03945
Langmuir 2019, 35, 4577–4588

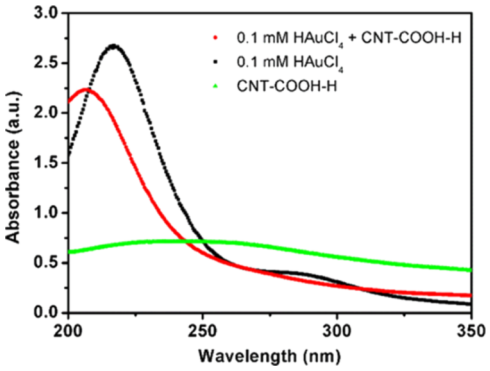

Figure 4. UV-vis spectra of untreated CNT-COOH-H, 0.1 mM $HAuCl_4$, and 0.1 mM $HAuCl_4$/CNT-COOH-H mixture.

growth in this type of plasma-assisted processes are different, but in some aspects closely related to nanoparticle formation using more standard methods (e.g., wet chemistry), which are still sources of great debates; for instance, the formation mechanism of the so-called "Turkevich synthesis",[59] which was initially proposed in 1951, is still largely under investigation.[47,60−62] It is convenient at this point to discuss separately the reduction/supply of Au monomers and the AuNP growth.

The reduction and supply of the Au monomer under plasma treatment can take place through different pathways (see Scheme 2). Solvated electrons (Scheme 2I) and hydrogen

Scheme 2. Potential Reaction Pathways in APP Synthesis of AuNP/CNT-COOH-H Hybrids

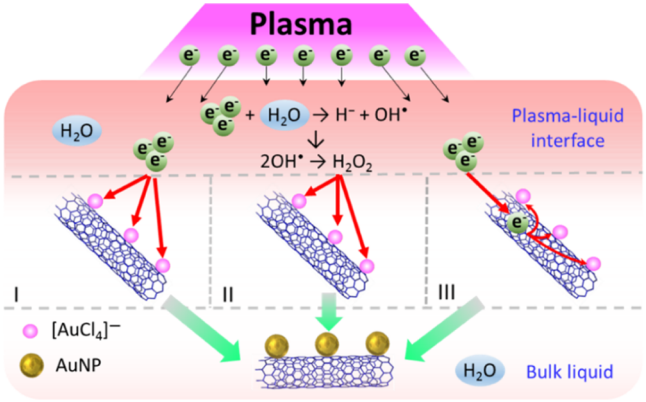

peroxide (Scheme 2II), both formed at the plasma−liquid interface, are known to be the main reducing agents as demonstrated by the relevant literature for comparable systems.[41,42,63] The reducing power of solvated electrons is limited to a volume close to the interface because of their short lifetime.[41,64] H_2O_2 on the other hand diffuses deeper into the bulk solution. The reducing power of hydrogen peroxide for $HAuCl_4$ is generally believed to prefer basic solutions, however, this does not necessarily mean that reduction is completely prevented in the acid environment; in fact there is experimental evidence that reduction is effective within minutes even with pH < 3.[41] A third possibility (Scheme 2III), determined by the CNT electron affinity and high conductivity, is that negative charges are captured and transported to the CNT surface binding sites, contributing to the surface reduction.[65] The mechanisms involved in the electron transport between CNT and AuNP has been reported by Khoo and Chelikowsky using density function calculations and the details can be found elsewhere.[66] We acknowledge that mechanism (III) is a speculation and would require a deeper in-depth investigation; however, we believe it is worthwhile mentioning as it could open up interesting synthetic prospects.

While it is difficult to quantitatively assess the dominant reduction mechanism, known reaction kinetic parameters can help to provide a qualitative description of the AuNP growth. The kinetics of electron-induced reaction is much faster than that of hydrogen peroxide and therefore we believe that the first pathway (i.e., because of solvated electrons) is mainly responsible for the initial growth through aggregation and coalescence close to the plasma−liquid interface. On the other hand, reduction due to H_2O_2 mainly drives coalescence and surface growth in the bulk of the solution.

With respect to AuNP growth, this is necessarily initiated by seed-formation through aggregation and coalescence, irrespective of the reduction pathways.[61] Aggregation initially leads to thermodynamically stable nuclei (a few Au atoms), which aggregate further or coalesce into stable seed particles. The formation of seed particles occurs both in the liquid phase as well as at the $[-COOAuCl_3]^-$ sites, the latter after reduction by either solvated electrons or hydrogen peroxide. Seed formation is then followed by surface growth where the remaining gold ions tend to be attracted and reduced in the electronic double layer. Coalescence is limited by colloidal stability, while surface growth continues until the monomer supply terminates, that is, when the salt is consumed.

This qualitative description of the growth mechanisms is drawn from studies of AuNP formation via standard wet chemical methods; however, it is supported by our findings. For instance, growth by coalescence ensures that NPs are grown at the CNT hybrid sites; this is because, without coalescence, NPs would be present also in solution, which is not what we have observed. The synthesis of AuNPs without CNTs (see Figure S3 in Supporting Information) shows that, for the concentrations considered here, colloidal stability is reached during coalescence and before agglomeration, this confirms that surface growth continues until the monomer supply is halted. AuNPs produced on the CNTs, for the same initial salt concentration, are generally smaller and more spherical than NPs produced without CNTs (also see Figure S3 in Supporting Information). This shows that CNTs impact the aggregation stage and cluster formation[61] and this is because the presence of hybrid CNT−Au sites forces the formation of a higher number of clusters reducing the mobility of a fraction of the gold salt precursor.

The main distinctive components of plasma-assisted synthesis are various: (i) fast kinetics offered by electron-induced reduction, (ii) on demand and localized production of the reducing agents (e.g., H_2O_2 and electrons), and (iii) contained reaction volume with strong concentration gradients. These allow tailoring the reaction pathways and better controlling the time/impact of the growth mechanisms, for example, the reduction of the reaction volume can preclude surface growth.[41] In the context of this part of work, we believe that the reaction kinetics of electron-induced reduction contributes to prevent seed particle formation in the solution.

In the following step, to further prove the proposed mechanisms, CNTs with a lower surface −COOH density (0.73%) (CNT-COOH-L, details see Experiment Section) and CNTs with −OH functional groups (CNT-OH, details see Experiment Section) were chosen for the synthesis of AuNP/

DOI: 10.1021/acs.langmuir.8b03945
Langmuir 2019, 35, 4577−4588

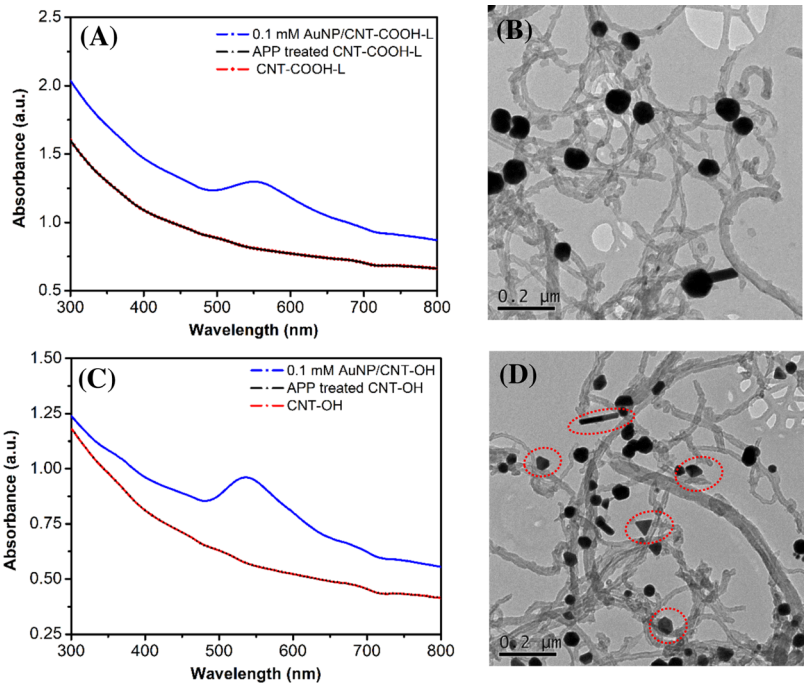

Figure 5. (A,C) UV−vis spectra of the 0.1 mM AuNP/CNT-COOH-L hybrid and 0.1 mM AuNP/CNT-OH hybrid; corresponding CNTs were used as references; (B,D) TEM images of 0.1 mM AuNP/CNT-COOH-L hybrid and 0.1 mM AuNP/CNT-OH hybrid.

CNT hybrids (see Table 2) following the same APP processing parameters.

The UV−vis and TEM results of these 0.1 mM AuNP/CNT-COOH-L and 0.1 mM AuNP/CNT-OH hybrids are shown in Figure 5. The UV−vis spectrum of 0.1 mM AuNP/CNT-COOH-L in Figure 5A shows that the LSPR peak wavelength of AuNP/CNT-COOH-L (552 nm) is red-shifted as compared to the 0.1 mM AuNP/CNT-COOH-H hybrid (531 nm). Similar to the 0.1 mM AuNP/CNT-COOH-H hybrid, the TEM image of 0.1 mM AuNP/CNT-COOH-L (Figure 5B) and corresponding shape projection analysis of AuNPs in this hybrid (see Figure S5, Supporting Information) also indicate that spherical AuNPs are uniformly attached to the surfaces of CNT-COOH-L. The average AuNPs size on CNT-COOH-L (95.1 ± 25.1 nm, see Figure S5 in Supporting Information) is much greater than that on CNT-COOH-H (28.7 ± 14.1 nm), which correlates to the red-shift of the LSPR peak. Observation from multiple TEM images of different magnifications (see Figure S6 in Supporting Information) also indicate there are less number of AuNPs formed on the surfaces of CNTs in the 0.1 mM AuNP/CNT-COOH-L hybrid than in the 0.1 mM AuNP/CNT-COOH-H. As discussed earlier, $AuCl_3$ on the surface of the CNT-COOH through ion exchange reaction with $-COO^-$ is believed to be preferential reduction and growth sites for AuNPs under such APP-assisted process. The much lower −COOH density of CNT-COOH-L provided much less sites compared to CNT-COOH-H, AuNPs with greater sizes could therefore be formed on the CNT-COOH-L surfaces by coalescence under the same initial $HAuCl_4$ concentration (same amount of monomers supplied to less CNT−Au sites).

However, when the surface functionalities of CNT were changed from −COOH to −OH groups, the formation mechanism of AuNP/CNT seems different from the results. Though a typical LSPR peak of AuNPs is still observed at 536 nm (Figure 5C), the AuNPs formed in the 0.1 mM AuNP/CNT-OH hybrid are presented in irregular shapes (hexagons, trapezoids, triangles, rods, and so forth.) with an average size of 50.3 ± 15.2 nm (see Figure S7 in Supporting Information) and some of them are loosely adsorbed/unattached to the CNT-OH (see NPs in red dash circles in Figure 5D). Figure 3 and literature have supported that $[AuCl_4]^-$ could react with CNT-COOH by ion exchanging reaction because of the ionization of −COOH in water as $-COO^-$ and H^+. While ion exchange is expected for CNT-COOH, no ion exchanging should in principle take place between CNT-OH and $[AuCl_4]^-$ because −OH cannot be ionized in water. This is confirmed by UV−vis spectra in Figure 6 when compared with Figure 4. When the

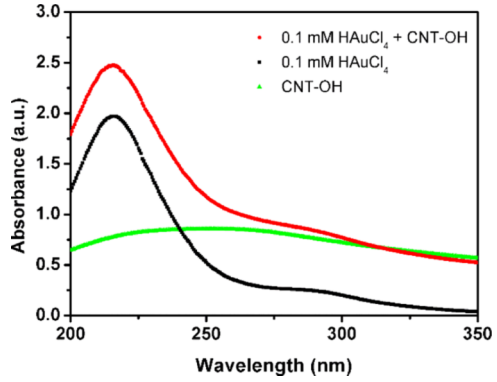

Figure 6. UV-vis spectra of untreated CNT-OH, 0.1 mM $HAuCl_4$, and 0.1 mM $HAuCl_4$/CNT-OH mixture.

$HAuCl_4$ was mixed with CNT-OH to form 0.1 mM $HAuCl_4$/CNT-OH mixture, both the 220 and 288 nm peaks of $[AuCl_4]^-$ remain constant in terms of the peak position and the intensity. The reduction and growth of AuNPs in this case mainly took place within the bulk solution, where the as-produced AuNPs then physically absorbed on the CNT-OH surfaces. This also explains AuNPs within the 0.1 mM AuNP/CNT-OH hybrid

DOI: 10.1021/acs.langmuir.8b03945
Langmuir 2019, 35, 4577−4588

shows similar morphologies (irregular shapes) to those produced without CNTs (Figure S4 in Supporting Information). Both the analysis of the 0.1 mM AuNP/CNT-COOH-L hybrid and 0.1 mM AuNP/CNT-OH hybrid support our proposed formation mechanisms leading to reduction and growth of AuNP in the presence of −COOH functionalized CNTs.

We finally focus on the investigation of important properties of the AuNP/CNT hybrids. We first compared the Raman scattering of AuNP/CNT-COOH-H hybrids synthesized from different initial $HAuCl_4$ concentrations (Figure 7A). Typical

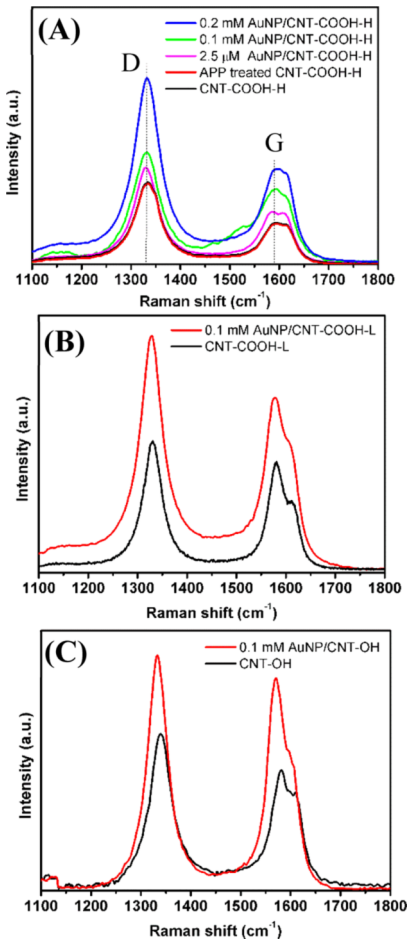

Figure 7. Raman spectra of (A) untreated CNT-COOH-H, APP treated CNT-COOH-H, and AuNP/CNT-COOH-H hybrids synthesized from different initial $HAuCl_4$ concentrations, (B) untreated CNT-COOH-L and 0.1 mM AuNP/CNT-COOH-L hybrid, and (C) untreated CNT−OH and 0.1 mM AuNP/CNT-OH hybrid.

disordered band (D band) (~1332 cm^{-1}) and graphene-like band (G band) (~1592 cm^{-1}) characteristic peaks are present for all samples and the APP treatment did not induce any further defects/modifications to the CNT-COOH-H. After the AuNPs formed on the CNT-COOH-H, samples exhibit significantly enhanced electromagnetic surface-enhanced Raman scattering (SERS), which can be essentially attributed to the LSPR oscillations of AuNPs under laser irradiation.[67] The greater SERS signal associated with samples produced from higher $HAuCl_4$ concentration correlates well with sample's greater particle size/number (also see Figure 2), as larger AuNPs normally possess higher SERS efficiency when the size of NPs falls in the range of 20−80 nm.[68] Similar to the 0.1 mM AuNP/CNT-COOH-H hybrid sample, the 0.1 mM AuNP/CNT-COOH-L hybrid (Figure 7B) and 0.1 mM AuNP/CNT-OH hybrid (Figure 7C) also demonstrated enhanced SERS properties compared to corresponding pure CNT samples because of the presence of AuNPs on their surface after APP treatment. Raman spectroscopy is widely used for medical diagnostic applications, such as sensing and imaging.[69] Because of their distinctive SERS signals, CNTs have attracted great research attention in the field of Raman spectrometric sensors.[12,70] From our Raman scattering results, the AuNP/CNT hybrids herein demonstrated greatly enhanced SERS signal as compared to untreated CNTs, hence, these hybrids would be promising materials to be used for medical diagnostic applications such as bio-imaging and sensing.[25−27]

Another very important property of our AuNP/CNT hybrids is their photothermal effect. The photothermal conversion efficiency of our hybrids was assessed in their aqueous media under the irradiation of laser. An 852 nm CW diode laser was selected because of its skin-penetrating ability within the biological window.[71] The photothermal conversion results of different AuNP/CNT-COOH-H hybrids are shown in Figure 8A, and corresponding pure AuNP colloids and CNT-COOH-H were used for comparison. The observed temperature increase represents the heat transfer from AuNP/

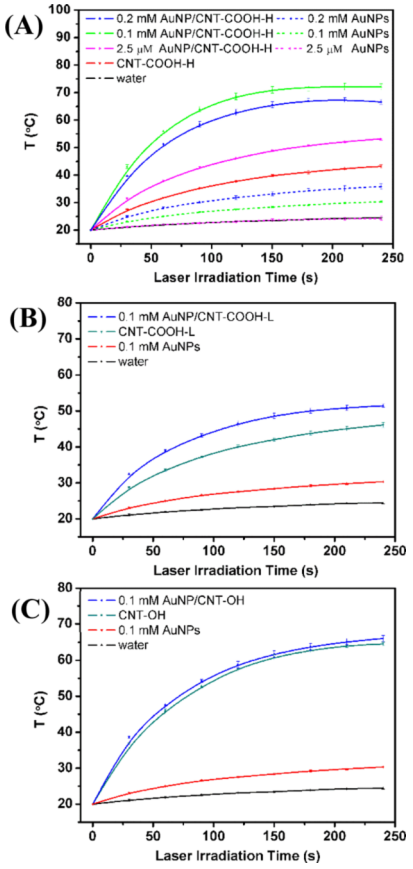

Figure 8. Photothermal effects of (A) AuNP/CNT-COOH-H hybrids synthesized from different initial $HAuCl_4$ concentrations, (B) 0.1 mM AuNP/CNT-COOH-L, and (C) 0.1 mM AuNP/CNT-OH under the irradiation of the 852 nm laser. Data points correspond to average values for three different measurements with corresponding standard deviation in the error bars.

DOI: 10.1021/acs.langmuir.8b03945
Langmuir 2019, 35, 4577−4588

CNT-COOH-H hybrids to the solution. All samples heated up from room temperature under the laser irradiation following the trend 0.1 mM AuNP/CNT-COOH-H > 0.2 mM AuNP/CNT-COOH-H > 2.5 μM AuNP/CNT-COOH-H > CNT-COOH-H > 0.2 mM AuNP> 0.1 mM AuNP > 2.5 μM AuNP. In particular, 0.1 and 0.2 mM AuNP/CNT-COOH-H hybrids heated up most rapidly (over 48 °C in 60 s), reaching the temperature range valid for photothermal cancer therapies.[72] It can also be clearly seen that all AuNP/CNT-COOH-H hybrids demonstrated enhanced photothermal conversion when compared to pure AuNP and as-received CNT-COOH-H under all of the three $HAuCl_4$ concentrations.

According to the TEM analysis (Figure 2), the presence of CNTs has a significant influence on the resultant AuNP shape and their distribution in the samples. Zedan et al. has shown that the photothermal effect of AuNP/nanocarbon hybrids can be affected by the shape and size of the AuNPs.[73] A more uniform distribution of the AuNPs on the CNTs with a tighter spherical shape distribution can therefore contribute to a more enhanced photothermal effect.

It is also worth noting that 0.2 mM AuNP/CNT-COOH-H hybrid shows a lower photothermal conversion efficiency as compared to the 0.1 mM AuNP/CNT-COOH-H hybrid. Because of the LSPR of AuNPs, the incident light irradiation on AuNPs could result in both light absorption and light scattering.[74] According to El-Sayed's calculation based on the Mie theory, larger AuNPs tend to have less light absorption but more scattering.[68] The decreased photothermal efficiency of 0.2 mM AuNP/CNT-COOH-H hybrid might be caused by the enhanced light scattering due to the larger AuNP size within the sample.[75]

We also compared the photothermal effects of the 0.1 mM AuNP/CNT hybrid synthesized from different CNTs. In Figure 8A, the 0.1 mM AuNP/CNT-COOH-H hybrid shows a temperature rise (ΔT) as high as 52.5 °C, which is higher than the sum of the ΔT of pure CNT-COOH-H (23.4 °C) and the ΔT of 0.1 mM AuNP (10.6 °C). When CNT-COOH-H was changed to CNT-COOH-L, the 0.1 mM AuNP/CNT-COOH-L hybrid also presents a reasonably high ΔT (~31.4 °C, see Figure 8B); however, considering that pure CNT-COOH-L alone showed a ΔT of 26.3 °C, the contribution of AuNPs to the photothermal enhancement within the hybrid is 5.1 °C—much lower than that for the 0.1 mM AuNP/CNT-COOH-H hybrid (19.1 °C). The observed trend appears to be again relevant to the size of AuNPs within these two hybrids; according to Figures 2 and 6, the AuNPs within the 0.1 mM AuNP/CNT-COOH-L hybrid has a much greater size than within the 0.1 mM AuNP/CNT-COOH-H hybrid and the enhanced light scattering of greater AuNPs could lead to decreased photothermal efficiency.[75] When comparing to CNT-OH, the 0.1 mM AuNP/CNT-OH hybrid only demonstrates a slight photothermal effect enhancement in the presence of AuNPs (ΔT = 1.5 °C, see Figure 8C). AuNPs LSPR is reported to promote the photo-absorption of nanocarbon and induce their plasmons,[76] therefore contributing to the overall enhanced photothermal effects. For −COOH-functionalized CNTs, the surface binding sites facilitated the charge transfer between AuNPs and CNTs through these sites. However, for AuNPs physically adsorbed on the surface of CNT-OH, the chances for electrons transfer would be negligible.

CONCLUSIONS

In summary, we have successfully demonstrated a single-step preparation of AuNP/CNT hybrids through a facile and rapid APP processing technology. The complicated interaction between multiphase materials (gas phase plasma, liquid, and solid state nanomaterials) and the associated plasma-chemistry contributed to the formation of AuNP/CNT-COOH hybrids via multiple reaction pathways have been elucidated in detail. The $[AuCl_4]^-$ and −COOH bindings serve as nucleation sites for the growth of AuNPs on the CNT-COOH surface and the resulting AuNP size increases with gold salt precursor concentration. The resulting hybrid structures, AuNP/CNT-COOH hybrids, demonstrated enhanced Raman scattering and high photothermal conversion efficiency, which are highly desirable for potential applications such as future multimodal cancer theranostic.

ASSOCIATED CONTENT

Supporting Information

The Supporting Information is available free of charge on the ACS Publications website at DOI: 10.1021/acs.langmuir.8b03945.

Photographs of CNT-COOH-H and AuNP/CNT-COOH-H hybrids solutions; TEM of pure CNT-COOH-H; shape project and size distribution of AuNPs within 2.5 μM, 0.1, and 0.2 mM AuNP/CNT-COOH-H hybrids; TEM images of pure AuNP samples and corresponding size distribution; shape project and size distribution of AuNPs within 0.1 mM AuNP/CNT-COOH-L; additional TEM images of the 0.1 mM AuNP/CNT-COOH-H and 0.1 mM AuNP/CNT-COOH-L; and shape project and size distribution of AuNPs within 0.1 mM AuNP/CNT-OH(PDF)

AUTHOR INFORMATION

Corresponding Author

*E-mail: d.sun@qub.ac.uk.

ORCID

Li Zhang: 0000-0002-0324-5092
Davide Mariotti: 0000-0003-1504-4383
Paul Maguire: 0000-0002-2725-4647
Dan Sun: 0000-0002-5100-2749

Notes

The authors declare no competing financial interest.

ACKNOWLEDGMENTS

The authors would like to acknowledge the Engineering and Physical Sciences Research Council (EPSRC) for funding support (EP/P00394X/1, EP/M015211/1, EP/S001069/1). D.S. thanks the China Scholarship Council (CSC) for the financial support.

REFERENCES

(1) Anselmo, A. C.; Mitragotri, S. Nanoparticles in the Clinic. *Bioeng. Transl. Med.* **2016**, *1*, 10−29.

(2) Tournebize, J.; Boudier, A.; Sapin-Minet, A.; Maincent, P.; Leroy, P.; Schneider, R. Role of Gold Nanoparticles Capping Density on Stability and Surface Reactivity to Design Drug Delivery Platforms. *ACS Appl. Mater. Interfaces* **2012**, *4*, 5790−5799.

(3) Popovtzer, R.; Agrawal, A.; Kotov, N. A.; Popovtzer, A.; Balter, J.; Carey, T. E.; Kopelman, R.; Popovtzer, A.; Balter, J.; Balter, J.; et al.

Targeted Gold Nanoparticles Enable Molecular CT Imaging of Cancer. *Nano Lett.* **2008**, *8*, 4593−4596.
(4) Zhao, Y.; Tong, L.; Li, Y.; Pan, H.; Zhang, W.; Guan, M.; Li, W.; Chen, Y.; Li, Q.; Li, Z.; et al. Lactose-Functionalized Gold Nanorods for Sensitive and Rapid Serological Diagnosis of Cancer. *ACS Appl. Mater. Interfaces* **2016**, *8*, 5813−5820.
(5) Fazal, S.; Jayasree, A.; Sasidharan, S.; Koyakutty, M.; Nair, S. V.; Menon, D. Green Synthesis of Anisotropic Gold Nanoparticles for Photothermal Therapy of Cancer. *ACS Appl. Mater. Interfaces* **2014**, *6*, 8080−8089.
(6) Liu, W.; Zhang, X.; Zhou, L.; Shang, L.; Su, Z. Reduced Graphene Oxide (RGO) Hybridized Hydrogel as a near-Infrared (NIR)/PH Dual-Responsive Platform for Combined Chemo-Photothermal Therapy. *J. Colloid Interface Sci.* **2019**, *536*, 160−170.
(7) Chen, H.; Liu, T.; Su, Z.; Shang, L.; Wei, G. 2D Transition Metal Dichalcogenide Nanosheets for Photo/Thermo-Based Tumor Imaging and Therapy. *Nanoscale Horiz.* **2018**, *3*, 74−89.
(8) Yu, X.; Zhang, W.; Zhang, P.; Su, Z. Fabrication Technologies and Sensing Applications of Graphene-Based Composite Films: Advances and Challenges. *Biosens. Bioelectron.* **2017**, *89*, 72−84.
(9) Zhao, X.; Zhang, P.; Chen, Y.; Su, Z.; Wei, G. Recent Advances in the Fabrication and Structure-Specific Applications of Graphene-Based Inorganic Hybrid Membranes. *Nanoscale* **2015**, *7*, 5080−5093.
(10) Wang, N.; Feng, Y.; Zeng, L.; Zhao, Z.; Chen, T. Functionalized Multiwalled Carbon Nanotubes as Carriers of Ruthenium Complexes to Antagonize Cancer Multidrug Resistance and Radioresistance. *ACS Appl. Mater. Interfaces* **2015**, *7*, 14933−14945.
(11) Wang, S.; Zhang, Q.; Yang, P.; Yu, X.; Huang, L.-Y.; Shen, S.; Cai, S. Manganese Oxide-Coated Carbon Nanotubes As Dual-Modality Lymph Mapping Agents for Photothermal Therapy of Tumor Metastasis. *ACS Appl. Mater. Interfaces* **2016**, *8*, 3736−3743.
(12) De la Zerda, A.; Zavaleta, C.; Keren, S.; Vaithilingam, S.; Bodapati, S.; Liu, Z.; Levi, J.; Smith, B. R.; Ma, T.-J.; Oralkan, O.; et al. Carbon Nanotubes as Photoacoustic Molecular Imaging Agents in Living Mice. *Nat. Nanotechnol.* **2008**, *3*, 557−562.
(13) Iyer, A. K.; Khaled, G.; Fang, J.; Maeda, H. Exploiting the Enhanced Permeability and Retention Effect for Tumor Targeting. *Drug Discovery Today* **2006**, *11*, 812−818.
(14) Kim, J.-W.; Galanzha, E. I.; Shashkov, E. V.; Moon, H.-M.; Zharov, V. P. Golden Carbon Nanotubes as Multimodal Photoacoustic and Photothermal High-Contrast Molecular Agents. *Nat. Nanotechnol.* **2009**, *4*, 688−694.
(15) Robinson, J. T.; Hong, G.; Liang, Y.; Zhang, B.; Yaghi, O. K.; Dai, H. In Vivo Fluorescence Imaging in the Second Near-Infrared Window with Long Circulating Carbon Nanotubes Capable of Ultrahigh Tumor Uptake. *J. Am. Chem. Soc.* **2012**, *134*, 10664−10669.
(16) Kostarelos, K. The Long and Short of Carbon Nanotube Toxicity. *Nat. Biotechnol.* **2008**, *26*, 774−776.
(17) Liu, Y.; Zhao, Y.; Sun, B.; Chen, C. Understanding the Toxicity of Carbon Nanotubes. *Acc. Chem. Res.* **2013**, *46*, 702−713.
(18) Deng, X.; Jia, G.; Wang, H.; Sun, H.; Wang, X.; Yang, S.; Wang, T.; Liu, Y. Translocation and Fate of Multi-Walled Carbon Nanotubes in Vivo. *Carbon* **2007**, *45*, 1419−1424.
(19) Fubini, B.; Ghiazza, M.; Fenoglio, I. Physico-Chemical Features of Engineered Nanoparticles Relevant to Their Toxicity. *Nanotoxicology* **2010**, *4*, 347−363.
(20) Poland, C. A.; Duffin, R.; Kinloch, I.; Maynard, A.; Wallace, W. A. H.; Seaton, A.; Stone, V.; Brown, S.; MacNee, W.; Donaldson, K. Carbon Nanotubes Introduced into the Abdominal Cavity of Mice Show Asbestos-like Pathogenicity in a Pilot Study. *Nat. Nanotechnol.* **2008**, *3*, 423−428.
(21) Sato, Y.; Yokoyama, A.; Shibata, K.-i.; Akimoto, Y.; Ogino, S.-i.; Nodasaka, Y.; Kohgo, T.; Tamura, K.; Akasaka, T.; Uo, M.; et al. Influence of Length on Cytotoxicity of Multi-Walled Carbon Nanotubes against Human Acute Monocytic Leukemia Cell Line THP-1 in Vitro and Subcutaneous Tissue of Rats in Vivo. *Mol. BioSyst.* **2005**, *1*, 176−182.
(22) Kang, S.; Lee, J.; Ryu, S.; Kwon, Y.; Kim, K.-H.; Jeong, D. H.; Paik, S. R.; Kim, B.-S. Gold Nanoparticle/Graphene Oxide Hybrid Sheets Attached on Mesenchymal Stem Cells for Effective Photothermal Cancer Therapy. *Chem. Mater.* **2017**, *29*, 3461−3476.
(23) Wang, X.; Wang, C.; Cheng, L.; Lee, S.-T.; Liu, Z. Noble Metal Coated Single-Walled Carbon Nanotubes for Applications in Surface Enhanced Raman Scattering Imaging and Photothermal Therapy. *J. Am. Chem. Soc.* **2012**, *134*, 7414−7422.
(24) Meng, L.; Xia, W.; Liu, L.; Niu, L.; Lu, Q. Golden Single-Walled Carbon Nanotubes Prepared Using Double Layer Polysaccharides Bridge for Photothermal Therapy. *ACS Appl. Mater. Interfaces* **2014**, *6*, 4989−4996.
(25) Wang, D.; Hou, C.; Meng, L.; Long, J.; Jing, J.; Dang, D.; Fei, Z.; Dyson, P. J. Stepwise Growth of Gold Coated Cancer Targeting Carbon Nanotubes for the Precise Delivery of Doxorubicin Combined with Photothermal Therapy. *J. Mater. Chem. B* **2017**, *5*, 1380−1387.
(26) Khan, S. A.; Kanchanapally, R.; Fan, Z.; Beqa, L.; Singh, A. K.; Senapati, D.; Ray, P. C. A Gold Nanocage-CNT Hybrid for Targeted Imaging and Photothermal Destruction of Cancer Cells. *Chem. Commun.* **2012**, *48*, 6711.
(27) Song, J.; Wang, F.; Yang, X.; Ning, B.; Harp, M. G.; Culp, S. H.; Hu, S.; Huang, P.; Nie, L.; Chen, J.; et al. Gold Nanoparticle Coated Carbon Nanotube Ring with Enhanced Raman Scattering and Photothermal Conversion Property for Theranostic Applications. *J. Am. Chem. Soc.* **2016**, *138*, 7005−7015.
(28) Caetano, F. R.; Felippe, L. B.; Zarbin, A. J. G.; Bergamini, M. F.; Marcolino-Junior, L. H. Gold Nanoparticles Supported on Multi-Walled Carbon Nanotubes Produced by Biphasic Modified Method and Dopamine Sensing Application. *Sens. Actuators, B* **2017**, *243*, 43−50.
(29) Lee, J.; Ahmed, S. R.; Oh, S.; Kim, J.; Suzuki, T.; Parmar, K.; Park, S. S.; Lee, J.; Park, E. Y. A Plasmon-Assisted Fluoro-Immunoassay Using Gold Nanoparticle-Decorated Carbon Nanotubes for Monitoring the Influenza Virus. *Biosens. Bioelectron.* **2014**, *64*, 311−317.
(30) Raghuveer, M. S.; Agrawal, S.; Bishop, N.; Ramanath, G. Microwave-Assisted Single-Step Functionalization and in Situ Derivatization of Carbon Nanotubes with Gold Nanoparticles. *Chem. Mater.* **2006**, *18*, 1390−1393.
(31) Leghrib, R.; Felten, A.; Demoisson, F.; Reniers, F.; Pireaux, J.-J.; Llobet, E. Room-Temperature, Selective Detection of Benzene at Trace Levels Using Plasma-Treated Metal-Decorated Multiwalled Carbon Nanotubes. *Carbon* **2010**, *48*, 3477−3484.
(32) Quinn, B. M.; Dekker, C.; Lemay, S. G. Electrodeposition of Noble Metal Nanoparticles on Carbon Nanotubes. *J. Am. Chem. Soc.* **2005**, *127*, 6146−6147.
(33) Qu, L.; Dai, L. Substrate-Enhanced Electroless Deposition of Metal Nanoparticles on Carbon Nanotubes. *J. Am. Chem. Soc.* **2005**, *127*, 10806−10807.
(34) Mariotti, D.; Sankaran, R. M. Microplasmas for Nanomaterials Synthesis. *J. Phys. D: Appl. Phys.* **2010**, *43*, 323001.
(35) Mariotti, D.; Belmonte, T.; Benedikt, J.; Velusamy, T.; Jain, G.; Švrček, V. Low-Temperature Atmospheric Pressure Plasma Processes for "Green" Third Generation Photovoltaics. *Plasma Processes Polym.* **2016**, *13*, 70−90.
(36) McKenna, J.; Patel, J.; Mitra, S.; Soin, N.; Švrček, V.; Maguire, P.; Mariotti, D. Synthesis and Surface Engineering of Nanomaterials by Atmospheric-Pressure Microplasmas. *Eur. Phys. J.: Appl. Phys.* **2011**, *56*, 24020.
(37) Svrcek, V.; Dohnalova, K.; Mariotti, D.; Trinh, M. T.; Limpens, R.; Mitra, S.; Gregorkiewicz, T.; Matsubara, K.; Kondo, M. Dramatic Enhancement of Photoluminescence Quantum Yields for Surface-Engineered Si Nanocrystals within the Solar Spectrum. *Adv. Funct. Mater.* **2013**, *23*, 6051−6058.
(38) Mitra, S.; Cook, S.; Švrček, V.; Blackley, R. A.; Zhou, W.; Kovač, J.; Cvelbar, U.; Mariotti, D. Improved Optoelectronic Properties of Silicon Nanocrystals/Polymer Nanocomposites by

DOI: 10.1021/acs.langmuir.8b03945
Langmuir 2019, 35, 4577−4588

Microplasma-Induced Liquid Chemistry. *J. Phys. Chem. C* **2013**, *117*, 23198−23207.
(39) Velusamy, T.; Liguori, A.; Macias-Montero, M.; Padmanaban, D. B.; Carolan, D.; Gherardi, M.; Colombo, V.; Maguire, P.; Svrcek, V.; Mariotti, D. Ultra-Small CuO Nanoparticles with Tailored Energy-Band Diagram Synthesized by a Hybrid Plasma-Liquid Process. *Plasma Processes Polym.* **2017**, *14*, 1600224.
(40) Bruggeman, P. J.; Kushner, M. J.; Locke, B. R.; Gardeniers, J. G. E.; Graham, W. G.; Graves, D. B.; Hofman-Caris, R. C. H. M.; Maric, D.; Reid, J. P.; Ceriani, E.; et al. Plasma-Liquid Interactions: A Review and Roadmap. *Plasma Sources Sci. Technol.* **2016**, *25*, 053002.
(41) Maguire, P.; Rutherford, D.; Macias-Montero, M.; Mahony, C.; Kelsey, C.; Tweedie, M.; Pérez-Martin, F.; McQuaid, H.; Diver, D.; Mariotti, D. Continuous In-Flight Synthesis for On-Demand Delivery of Ligand-Free Colloidal Gold Nanoparticles. *Nano Lett.* **2017**, *17*, 1336−1343.
(42) Patel, J.; Němcová, L.; Maguire, P.; Graham, W. G.; Mariotti, D. Synthesis of Surfactant-Free Electrostatically Stabilized Gold Nanoparticles by Plasma-Induced Liquid Chemistry. *Nanotechnology* **2013**, *24*, 245604.
(43) Huang, X. Z.; Zhong, X. X.; Lu, Y.; Li, Y. S.; Rider, A. E.; Furman, S. A.; Ostrikov, K. Plasmonic Ag Nanoparticles via Environment-Benign Atmospheric Microplasma Electrochemistry. *Nanotechnology* **2013**, *24*, 095604.
(44) Wang, R.; Zuo, S.; Zhu, W.; Zhang, J.; Fang, J. Rapid Synthesis of Aqueous-Phase Magnetite Nanoparticles by Atmospheric Pressure Non-Thermal Microplasma and Their Application in Magnetic Resonance Imaging. *Plasma Processes Polym.* **2014**, *11*, 448−454.
(45) Du, C.; Xiao, M. Cu_2O Nanoparticles Synthesis by Micro-plasma. *Sci. Rep.* **2014**, *4*, 7339.
(46) Yan, T.; Zhong, X.; Rider, A. E.; Lu, Y.; Furman, S. A.; Ostrikov, K. Microplasma-chemical Synthesis and Tunable Real-time Plasmonic Responses of Alloyed Au_xAg_{1-x} Aanoparticles. *Chem. Commun.* **2014**, *50*, 3144−3147.
(47) Bastús, N. G.; Comenge, J.; Puntes, V. Kinetically Controlled Seeded Growth Synthesis of Citrate-Stabilized Gold Nanoparticles of up to 200 Nm: Size Focusing versus Ostwald Ripening. *Langmuir* **2011**, *27*, 11098−11105.
(48) Haiss, W.; Thanh, N. T. K.; Aveyard, J.; Fernig, D. G. Determination of Size and Concentration of Gold Nanoparticles from UV−Vis Spectra. *Anal. Chem.* **2007**, *79*, 4215−4221.
(49) Datsyuk, V.; Kalyva, M.; Papagelis, K.; Parthenios, J.; Tasis, D.; Siokou, A.; Kallitsis, I.; Galiotis, C. Chemical Oxidation of Multiwalled Carbon Nanotubes. *Carbon* **2008**, *46*, 833−840.
(50) Yang, E.; Chou, H.; Tsumura, S.; Nagatsu, M. Surface Properties of Plasma-Functionalized Graphite-Encapsulated Gold Nanoparticles Prepared by a Direct Current Arc Discharge Method. *J. Phys. D: Appl. Phys.* **2016**, *49*, 185304.
(51) Minicò, S.; Scirè, S.; Crisafulli, C.; Galvagno, S. Influence of Catalyst Pretreatments on Volatile Organic Compounds Oxidation over Gold/Iron Oxide. *Appl. Catal., B* **2001**, *34*, 277−285.
(52) Goguet, A.; Ace, M.; Saih, Y.; Sa, J.; Kavanagh, J.; Hardacre, C. Remarkable Stability of Ionic Gold Supported on Sulfated Lanthanum Oxide. *Chem. Commun.* **2009**, 4889−4891.
(53) Boyen, H.-G.; Kästle, G.; Weigl, F.; Koslowski, B.; Dietrich, C.; Ziemann, P.; Spatz, J. P.; Riethmüller, S.; Hartmann, C.; Möller, M. Oxidation-Resistant Gold-55 Clusters. *Science* **2002**, *297*, 1533−1536.
(54) Suarez-Martinez, I.; Bittencourt, C.; Ke, X.; Felten, A.; Pireaux, J. J.; Ghijsen, J.; Drube, W.; Van Tendeloo, G.; Ewels, C. P. Probing the Interaction between Gold Nanoparticles and Oxygen Function-alized Carbon Nanotubes. *Carbon* **2009**, *47*, 1549−1554.
(55) Shieh, Y.-T.; Liu, G.-L.; Wu, H.-H.; Lee, C.-C. Effects of Polarity and PH on the Solubility of Acid-Treated Carbon Nanotubes in Different Media. *Carbon* **2007**, *45*, 1880−1890.
(56) *Ion Exchange: Science and Technology*; Rodrigues, A. E., Ed.; Springer Science & Business Media, 2012.
(57) Zhang, R.; Wang, Q.; Zhang, L.; Yang, S.; Yang, Z.; Ding, B. The Growth of Uncoated Gold Nanoparticles on Multiwalled Carbon Nanotubes. *Colloids Surf., A* **2008**, *312*, 136−141.
(58) Kim, Y.-G.; Oh, S.-K.; Crooks, R. M. Preparation and Characterization of 1−2 nm Dendrimer-Encapsulated Gold Nano-particles Having Very Narrow Size Distributions. *Chem. Mater.* **2004**, *16*, 167−172.
(59) Turkevich, J.; Stevenson, P. C.; Hillier, J. A Study of the Nucleation and Growth Processes in the Synthesis of Colloidal Gold. *Discuss. Faraday Soc.* **1951**, *11*, 55−75.
(60) Wuithschick, M.; Witte, S.; Kettemann, F.; Rademann, K.; Polte, J. Illustrating the Formation of Metal Nanoparticles with a Growth Concept Based on Colloidal Stability. *Phys. Chem. Chem. Phys.* **2015**, *17*, 19895−19900.
(61) Wuithschick, M.; Birnbaum, A.; Witte, S.; Sztucki, M.; Vainio, U.; Pinna, N.; Rademann, K.; Emmerling, F.; Kraehnert, R.; Polte, J. Turkevich in New Robes: Key Questions Answered for the Most Common Gold Nanoparticle Synthesis. *ACS Nano* **2015**, *9*, 7052−7071.
(62) Kimling, J.; Maier, M.; Okenve, B.; Kotaidis, V.; Ballot, H.; Plech, A. Turkevich Method for Gold Nanoparticle Synthesis Revisited. *J. Phys. Chem. B* **2006**, *110*, 15700−15707.
(63) Bratescu, M. A.; Cho, S.-P.; Takai, O.; Saito, N. Size-Controlled Gold Nanoparticles Synthesized in Solution Plasma. *J. Phys. Chem. C* **2011**, *115*, 24569−24576.
(64) Rumbach, P.; Bartels, D. M.; Sankaran, R. M.; Go, D. B. The Solvation of Electrons by an Atmospheric-Pressure Plasma. *Nat. Commun.* **2015**, *6*, 7248.
(65) Dudin, P. V.; Unwin, P. R.; Macpherson, J. V. Electrochemical Nucleation and Growth of Gold Nanoparticles on Single-Walled Carbon Nanotubes: New Mechanistic Insights. *J. Phys. Chem. C* **2010**, *114*, 13241−13248.
(66) Khoo, K. H.; Chelikowsky, J. R. Electron Transport across Carbon Nanotube Junctions Decorated with Au Nanoparticles: Density Functional Calculations. *Phys. Rev. B: Condens. Matter Mater. Phys.* **2009**, *79*, 205422.
(67) Chu, H.; Wang, J.; Ding, L.; Yuan, D.; Zhang, Y.; Liu, J.; Li, Y. Decoration of Gold Nanoparticles on Surface-Grown Single-Walled Carbon Nanotubes for Detection of Every Nanotube by Surface-Enhanced Raman Spectroscopy. *J. Am. Chem. Soc.* **2009**, *131*, 14310−14316.
(68) Jain, P. K.; Lee, K. S.; El-Sayed, I. H.; El-Sayed, M. A. Calculated Absorption and Scattering Properties of Gold Nano-particles of Different Size, Shape, and Composition: Applications in Biological Imaging and Biomedicine. *J. Phys. Chem. B* **2006**, *110*, 7238−7248.
(69) Kong, K.; Kendall, C.; Stone, N.; Notingher, I. Raman Spectroscopy for Medical Diagnostics - From in-Vitro Biofluid Assays to in-Vivo Cancer Detection. *Adv. Drug Delivery Rev.* **2015**, *89*, 121−134.
(70) Liu, Z.; Tabakman, S.; Welsher, K.; Dai, H. Carbon Nanotubes in Biology and Medicine: In Vitro and in Vivo Detection, Imaging and Drug Delivery. *Nano Res.* **2009**, *2*, 85−120.
(71) Moon, H. K.; Lee, S. H.; Choi, H. C. In Vivo Near-Infrared Mediated Tumor Destruction by Photothermal Effect of Carbon Nanotubes. *ACS Nano* **2009**, *3*, 3707−3713.
(72) Jaque, D.; Martínez Maestro, L.; del Rosal, B.; Haro-Gonzalez, P.; Benayas, A.; Plaza, J. L.; Martín Rodríguez, E.; García Solé, J. Nanoparticles for Photothermal Therapies. *Nanoscale* **2014**, *6*, 9494−9530.
(73) Zedan, A. F.; Moussa, S.; Terner, J.; Atkinson, G.; El-Shall, M. S. Ultrasmall Gold Nanoparticles Anchored to Graphene and Enhanced Photothermal Effects by Laser Irradiation of Gold Nanostructures in Graphene Oxide Solutions. *ACS Nano* **2013**, *7*, 627−636.
(74) Huang, X.; El-Sayed, M. A. Gold Nanoparticles: Optical Properties and Implementations in Cancer Diagnosis and Photo-thermal Therapy. *J. Adv. Res.* **2010**, *1*, 13−28.
(75) Jiang, K.; Smith, D. A.; Pinchuk, A. Size-Dependent Photothermal Conversion Efficiencies of Plasmonically Heated Gold Nanoparticles. *J. Phys. Chem. C* **2013**, *117*, 27073−27080.

DOI: 10.1021/acs.langmuir.8b03945
Langmuir 2019, 35, 4577−4588

(76) Alonso-Gonzalez, P.; Nikitin, A. Y.; Golmar, F.; Centeno, A.; Pesquera, A.; Velez, S.; Chen, J.; Navickaite, G.; Koppens, F.; Zurutuza, A. Controlling Graphene Plasmons with Resonant Metal Antennas and Spatial Conductivity Patterns. *Science* **2014**, *344*, 1369−1373.

DOI: 10.1021/acs.langmuir.8b03945
Langmuir 2019, 35, 4577−4588